Interstitial Mo-Assisted Photovoltaic Effect in Multilayer $MoSe_2$ Phototransistors

Sunkook Kim, Jesse Maassen, Jiyoul Lee, Seung Min Kim, Gyuchull Han, Junyeon Kwon, Seongin Hong, Jozeph Park, Na Liu, Yun Chang Park, Inturu Omkaram, Jong-Soo Rhyee, Young Ki Hong, and Youngki Yoon**

Thin-film transistors (TFTs) based on multilayer molybdenum diselenide ($MoSe_2$) synthesized by modified atmospheric pressure chemical vapor deposition (APCVD) exhibit outstanding photoresponsivity (103.1 A W^{-1}), while it is generally believed that optical response of multilayer transition metal dichalcogenides (TMDs) is significantly limited due to their indirect bandgap and inefficient photoexcitation process. Here, the fundamental origin of such a high photoresponsivity in the synthesized multilayer $MoSe_2$ TFTs is sought. A unique structural characteristic of the APCVD-grown $MoSe_2$ is observed, in which interstitial Mo atoms exist between basal planes, unlike usual 2H phase TMDs. Density functional theory calculations and photoinduced transfer characteristics reveal that such interstitial Mo atoms form photoreactive electronic states in the bandgap. Models indicate that huge photoamplification is attributed to trapped holes in subgap states, resulting in a significant photovoltaic effect. In this study, the fundamental origin of high responsivity with synthetic $MoSe_2$ phototransistors is identified, suggesting a novel route to high-performance, multifunctional 2D material devices for future wearable sensor applications.

2D layered materials such as transition metal dichalcogenides (TMDs) are significant contenders for future photosensors[1] due to their superior electrical and optical properties as well as mechanical stability,[2] and the optical properties of 2D materials can be even modulated by using metal nanostructures.[3] Over the years, the photoresponsivity – a figure of merit for photosensors – of multilayer TMDs has remained relatively low, unlike that of monolayer TMDs, due to their indirect bandgap and inefficient photoexcitation process.[2a,4] However, multilayer TMDs have clear advantages over their monolayer counterparts for practical applications in terms of favorable fabrication processes, large density of states (DOS), and wide spectral responses.[4b,5] Recently, it has been reported that multilayer molybdenum diselenide ($MoSe_2$) can exhibit large photoresponsivity,[6] while that of multilayer molybdenum disulfide (MoS_2) is significantly limited under photodetecting device architectures.[4b,7] Notably, it is known that natural $MoSe_2$ flakes do not exist,[8] and therefore, all previous measurements have been based on synthetic $MoSe_2$.[9] Here, our central interest lies in the fundamental origin of large photoresponsivity with synthesized $MoSe_2$, compared to naturally occurring TMDs such as MoS_2 flakes. If it can be identified, a novel route can be paved for highly sensitive photodetectors by engineering synthetic $MoSe_2$, which is, however, inherently unachievable with natural MoS_2 flakes due to the uncontrolled growth condition and possible variations.

Prof. S. Kim, J. Kwon, S. Hong, Dr. J. Park, Dr. N. Liu, Dr. I. Omkaram, Dr. Y. K. Hong
Multi-Functional Nano/Bio Electronics Laboratory
Sungkyunkwan University
Gyeonggi 16419, South Korea
E-mail: imhyke0419@gmail.com

Prof. J. Maassen
Department of Physics and Atmospheric Science
Dalhousie University
Halifax NS B3H 4R2, Canada

Prof. J. Lee
Department of Graphic Arts Information Engineering
Pukyong National University
Busan 608-739, South Korea

Dr. S. M. Kim
Institute of Advanced Composite Materials
Korea Institute of Science and Technology
Jeonbuk 565-905, South Korea

G. Han, Prof. Y. Yoon
Department of Electrical and Computer Engineering and Waterloo Institute for Nanotechnology (WIN)
University of Waterloo
Waterloo ON N2L 3G1, Canada
E-mail: youngki.yoon@uwaterloo.ca

Dr. Y. C. Park
Measurement & Analysis Team
National Nanofab Center
Daejeon 34141, South Korea

Prof. J.-S. Rhyee
Department of Applied Physics
Kyung Hee University
Gyeonggi 17104, South Korea

DOI: 10.1002/adma.201705542

Interestingly, although typical natural MoS_2-based phototransistors exhibit significantly low photoresponsivity, we found that a limited number of devices based on the same material show remarkably better optical behaviors. Such performance deviation can be expected with MoS_2 flakes due to nonuniform growth conditions in the natural environment (where high-pressure and high-temperature environments are typically achieved). Since this can provide us a clue to understand the optical properties of synthetic $MoSe_2$, first we have investigated the microstructure of natural MoS_2. As a result, we could observe additional atomic layers between the basal planes, which are normally empty regions in the 2H hexagonal structure, for the MoS_2 flakes showing relatively high photoresponsivity. More importantly, similar interstitial atoms can also be found with $MoSe_2$ synthesized by modified atmospheric pressure chemical vapor deposition (APCVD). To identify the interstitial atoms observed in the synthetic $MoSe_2$, we have performed density functional theory (DFT) calculations, and the results suggest that the interstitial atoms are Mo interstitials (Mo_{int}). DFT simulations further reveal that gap states can be induced by Mo_{int}, which is also experimentally supported from the measurement of photoinduced transfer characteristics. Moreover, we modeled the conductivity increase with illumination (photoconductive (PC) effect) and the threshold voltage shift due to the local accumulation of charges (photovoltaic (PV) effect) independently to further understand the measured data, and found that the trap states induced by Mo_{int} are the origin of high photoresponsivity in APCVD-grown $MoSe_2$ phototransistors, where the PV effect is predominant over the PC effect. In this study, we systematically identified the origin of high photoresponsivity in synthetic $MoSe_2$ phototransistors based on our comprehensive approach, including material growth, device fabrication, advanced experimental analyses, as well as DFT simulations and modeling, thereby suggesting a novel route to realize highly sensitive phototransistors using APCVD-grown multilayer $MoSe_2$.

Figure 1a shows the average photoresponsivity (R; the ratio of photocurrent to the incident power) from 10 representative MoS_2 (■) and $MoSe_2$ (Δ) phototransistors, which turns out to be 0.17 ± 0.05 and 85.3 ± 11.86 A W^{-1}, respectively. Relatively lower R of multilayer MoS_2 is in good agreement with previous reports.[4b,7] However, we could also find a MoS_2 phototransistor exhibiting an unusually high R value of 10.1 A W^{-1} (□), which is about two orders of magnitude larger than the typical values from multilayer MoS_2 devices. While any noticeable interstitial defect was not observed in a scanning transmission electron microscope (STEM) image (Figure 1b) for a typical multilayer MoS_2 phototransistor, distinct interstitial atoms (red-dashed ellipse) could be clearly observed from a cross-sectional high-resolution transmission electron microscopy (HRTEM) image

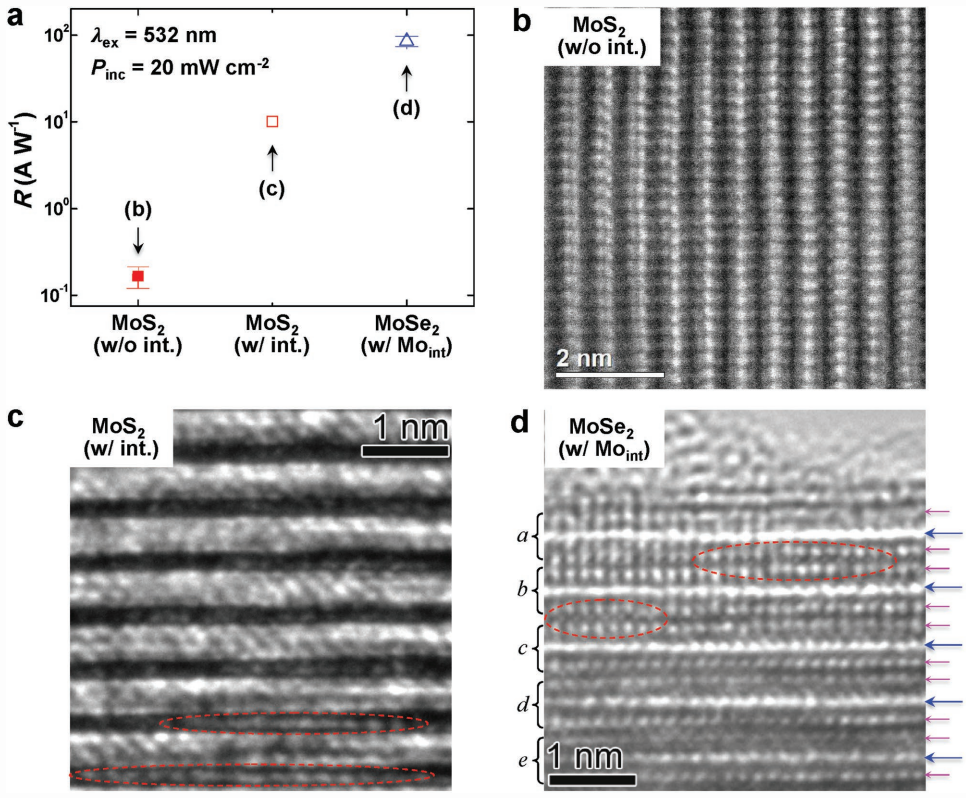

Figure 1. Relation between photoresponsivity and interstitial atoms in MoX_2 (X = Se, S). a) Comparison of the measured photoresponsivity (R) of natural MoS_2 flakes with and without interstitial atoms as well as that of synthetic $MoSe_2$ with Mo interstitial (Mo_{int}). b) Cross-sectional STEM image of MoS_2 without interstitials. c) Aberration-corrected HRTEM image of MoS_2 with interstitials (red-dashed ellipses). d) Aberration-corrected HRTEM images of $MoSe_2$, exhibiting interstitial Mo atoms. Red-dashed ellipses indicate additional atomic layers between the $MoSe_2$ basal planes. A total of 5 layers of 2H stacking structure in $MoSe_2$ are clearly identified, which were denoted by braces and corresponding italicized characters. Blue and pink arrows designate atomic lines of Mo and Se, respectively.

(Figure 1c) for the MoS_2 device showing a relatively large R value. Similarly, the layered structure of our synthetic $MoSe_2$ is also exhibited in the aberration-corrected HRTEM image (Figure 1d). Each layer is stacked following the ABABAB sequence, which is consistent with the X-ray diffraction (XRD) and Raman spectroscopy analyses as shown in Figure S1 (Supporting Information), confirming that as a whole our APCVD-grown $MoSe_2$ has a 2H hexagonal structure. In Figure 1d, a total of 5 layers of 2H stacking structure are clearly identified with braces and corresponding italicized characters, and a couple of interstitial atoms were found between *a*- and *b*-layers (red-dashed ellipse) and also another group of interstitials between *b*- and *c*-layers.

Figure 2a,b shows the transfer characteristics of multilayer $MoSe_2$ and MoS_2 thin-film transistor (TFT), respectively, under illumination with various incident optical power densities (P_{inc})

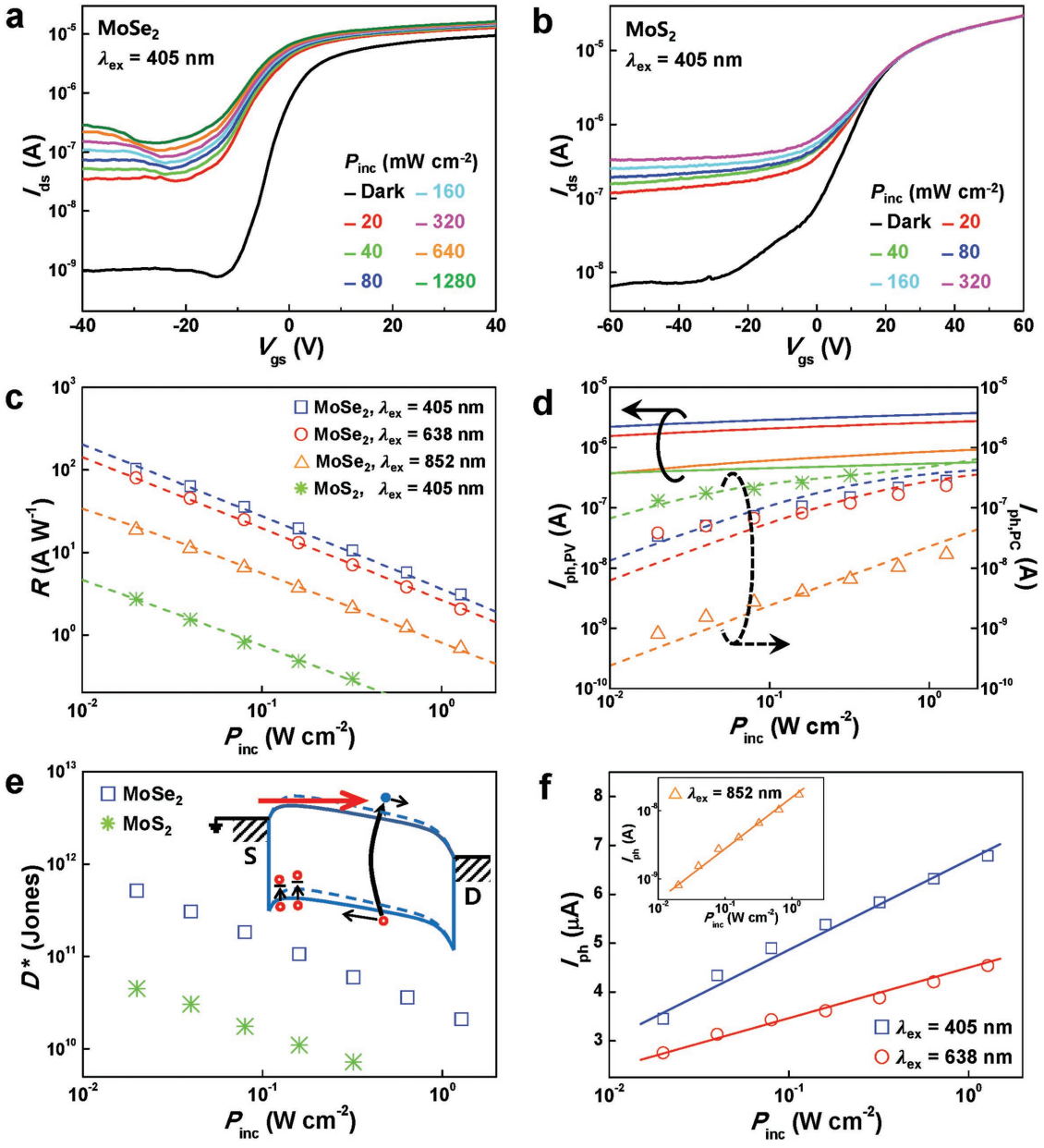

Figure 2. Photoresponsive behavior of APCVD-grown $MoSe_2$ TFTs. a,b) I_{ds}–V_{gs} characteristics of multilayer (a) $MoSe_2$ and (b) MoS_2 phototransistors under illumination with a wavelength of 405 nm and various incident optical power densities. c) Measured (symbols) and modeled (dashed lines) photoresponsivity (R) as a function of P_{inc} for the $MoSe_2$ and MoS_2 phototransistors. A maximum value of 103.1 A W^{-1} is obtained at $P_{inc} = 20$ mW cm^{-2} and $\lambda_{ex} = 405$ nm with $MoSe_2$. d) The modeled $I_{ph,PV}$ (solid lines) and $I_{ph,PC}$ (dashed lines) plotted independently for the devices shown in (a) and (b) (the same colors are used as in (c) for various wavelengths). The symbols are taken from the measurements in the off states ($V_{gs} = -40$ V) for $I_{ph,PC}$. e) (Main panel) Calculated specific detectivity (D^*) for $MoSe_2$ and MoS_2 photodetectors at $\lambda_{ex} = 405$ nm. (Inset) Schematic energy band diagram, showing the mechanism of the photovoltaic (PV) effect. Filled and open circles denote electrons and holes, respectively. f) Photocurrent response to light intensity at $\lambda_{ex} = 405$, 638 nm (main panel) and 852 nm (inset).

at an excitation wavelength (λ_{ex}) of 405 nm and V_{ds} = 1 V. It should be noted that a typical natural flake of MoS_2 (as shown in Figure 1b) has been used here to provide representative optical behaviors of multilayer MoS_2 TFTs. While both materials show significant increase of off-state current (at low V_{gs}) under light compared to the dark states, only $MoSe_2$ exhibits clear response to illumination at on state (high V_{gs}) as shown in Figure 2a, whereas on current of the MoS_2 TFT remains nearly unchanged under the exposure to light (Figure 2b). In Figure 2c, we compare the photoresponsivity of $MoSe_2$ and MoS_2 for various P_{inc}, where symbols represent the experimentally obtained values. A maximum photoresponsivity of 103.1 A W^{-1} was achieved with $MoSe_2$ at P_{inc} = 20 mW cm^{-2} and λ_{ex} = 405 nm, which is ≈40 times larger than that of natural multilayer MoS_2 phototransistors.

In order to understand the large photoresponsivity in the synthetic multilayer $MoSe_2$ TFTs, we have investigated the photocurrent induced by the PC effect ($I_{ph,PC}$) and the PV effect ($I_{ph,PV}$) independently in Figure 2d. Under illumination, electron–hole pairs are generated and the conductivity of the channel material is increased. This conductivity increase due to photoinduced excess carriers is the PC effect, and the consequent photocurrent is calculated by $I_{ph,PC} = \left(\frac{W}{L}\right) V_{ds} \Delta\sigma$, where W, L, V_{ds}, and $\Delta\sigma$ are the width and length of the device, the source–drain voltage, and the conductivity increase due to light illumination, respectively.[10] On the other hand, the PV effect is modeled with the threshold voltage (V_{th}) shift caused by accumulation of holes and barrier lowering, which is given by $I_{ph,PV} = g_m \Delta V_{th}$, where g_m is the transconductance in the dark and ΔV_{th} is the threshold voltage shift induced by illumination.[11] While the excess electrons in the conduction band can easily move from the channel to the drain, the motion of the excess holes in the valence band can be hampered by a barrier near the source–channel junction, leading to the local accumulation of holes. Moreover, these excess holes can be captured by trap states, resulting in the suppression of the potential barrier and the increase of electron injection from the source, as depicted in the inset of Figure 2e.

To analyze the measured data using our models (details of the models are described in the Experimental Section), first we have plotted $I_{ph,PC}$ in Figure 2d (dashed lines) by fitting τ_r, τ_t/τ_g, and P_t with experimental data (symbols; obtained from Figure 2a,b and Figure S3 (Supporting Information) in the off state), where τ_r is the recombination lifetime, P_t is the trap density, τ_t and τ_g are the trapping and escaping time of holes into and from the trap states, respectively.[10] Then, photoresponsivity values are fitted in Figure 2c (dashed lines), where both $I_{ph,PC}$ and $I_{ph,PV}$ are considered ($I_{ph} = I_{ph,PC} + I_{ph,PV}$), by introducing a parameter χ_{BL} describing barrier-lowering efficiency. Finally, we obtained $I_{ph,PV}$ from $I_{ph} - I_{ph,PC}$ and plotted it in Figure 2d (solid lines) to compare with $I_{ph,PC}$. Interestingly, our results indicate that, although the photoconductive current is larger with MoS_2, the synthetic $MoSe_2$ shows a significantly larger PV effect, resulting in remarkably higher photoresponsivity in the $MoSe_2$ TFTs. Notably, $I_{ph,PV}$ is larger than $I_{ph,PC}$ by 92 times with $MoSe_2$ at P_{inc} = 20 mW cm^{-2} and λ_{ex} = 405 nm, whereas $I_{ph,PV}/I_{ph,PC}$ of MoS_2 remains much lower for the entire range of P_{inc} considered. The fitted parameters (τ_r, τ_t/τ_g, P_t, χ_{BL}; the values are provided in the Experimental Section) indicate that a greater number of states exists energetically deeper in the bandgap region for the synthetic $MoSe_2$, resulting in shorter recombination lifetime (hence smaller $I_{ph,PC}$) and longer escaping time for holes from the trap states (hence larger $I_{ph,PV}$), compared to those in MoS_2 flakes.

Specific detectivity (D^*) is another figure of merit for photodetectors, which indicates the sensitivity of detectors and is given by $D^* = \frac{RA^{1/2}}{(2qI_{dark})^{1/2}}$, where R is the responsivity, A is the area of detector, q is the unit charge, and I_{dark} is the dark current.[12] Figure 2e shows the calculated D^* of the synthesized $MoSe_2$ and natural MoS_2 phototransistors at λ_{ex} = 405 nm, which clearly exhibits that the specific detectivity of the $MoSe_2$ is larger than that of MoS_2 by one order of magnitude. Linearity and robust light switching behaviors are also important features required for practical photodetector applications. The main panel in Figure 2f shows the linear response of I_{ph} to light intensity for our multilayer $MoSe_2$ phototransistor at λ_{ex} = 405 and 638 nm in the on state (V_{gs} = 40 V). The linearity at λ_{ex} = 852 nm was plotted separately in the inset of Figure 2f considering the photoconductive current in the off state (V_{gs} = −40 V) due to the limited PV effect in the on state (Figure S3b, Supporting Information). The time-resolved photoswitching behavior of the $MoSe_2$ TFT is also presented in Figure S4 (Supporting Information). The photoresponse remains almost identical for multiple cycles of light switching with intervals of 20 s, which demonstrates the robustness and feasibility of our $MoSe_2$ phototransistors for high-performance photodetectors.

In Figure 1d, we could observe interstitial atoms between the basal planes of APCVD-grown $MoSe_2$, however we could not identify the kind of atoms using spectroscopy methods. Here, we identify the kind of interstitial atoms observed in multilayer $MoSe_2$ first, and then discuss the role of such interstitials in phototransistors. Considering our unique growth condition of $MoSe_2$, in which the material is grown on a 100 nm thick Mo-coated silicon (Si) substrates (i.e., Mo-rich condition), it is reasonable to believe that the observed additional atoms in $MoSe_2$ are Mo_{int}, and interstitial Se (Se_{int}) is very unlikely to be formed due to the deficiency of Se atom. In order to justify our claim, we have calculated defect formation energies using DFT simulations[13] (details of the calculation approach are provided in the Experimental Section). The defects considered include Mo_{int}, Se_{int}, Mo vacancy (Mo_{vac}), and Se vacancy (Se_{vac}). **Figure 3**a shows the calculated formation energy of the defects. We consider two cases: when the simulation cell is allowed ("free cell"), or not allowed ("fixed cell"), to change shape/volume during the structural relaxation. The "free cell" DFT results indicate that Se_{int} is the interstitial with lower formation energy than Mo_{int}. However, a key observation from the simulations is that the introduction of Se_{int} leads to a significant reconstruction of the $MoSe_2$ structure during the atomic relaxation (which seeks to minimize the total energy). With Mo_{int}, and all other simulated defects except Se_{int}, the $MoSe_2$ remains hexagonal after relaxation, while with Se_{int}, there is significant reconstruction resulting in a triclinic lattice. Similar materials, such as MoS_2, are known to be susceptible to phase transitions,[14] which can be controllable and reversible.[15]

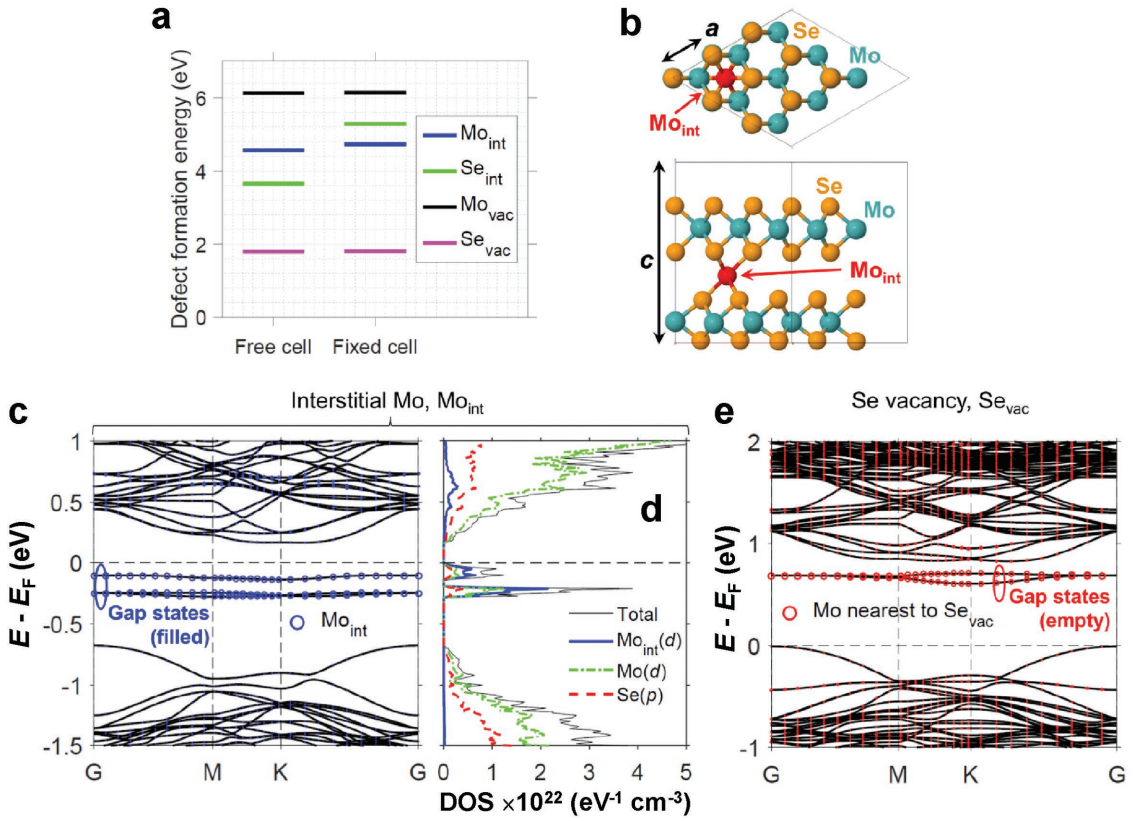

Figure 3. Properties of intrinsic defects in synthetic $MoSe_2$. a) DFT calculated defect formation energies in bulk $MoSe_2$ under Mo-rich condition. Free (fixed) cell corresponds to the case when the simulation cell is (not) allowed to change shape/volume during the structural relaxation. b) Atomic structure of a $3 \times 3 \times 1$ supercell with one interstitial Mo atom (Mo_{int}). c) Band structure of a $4 \times 4 \times 1$ supercell with one Mo_{int}, with contributions from the Mo_{int} (d-orbitals) depicted by circles. d) DOS versus energy relative to the Fermi level, with partial DOS contributions from the Mo_{int} atom (d-orbitals), Mo atoms (d-orbitals), and Se atoms (p-orbitals). Note that the selected orbital projections are the dominant contributions from each atom. e) Band structure of a $4 \times 4 \times 1$ supercell with one Se vacancy, with contributions from the three nearest neighbor Mo atoms (d-orbitals) depicted by circles.

Our XRD analysis, provided in the Supporting Information, confirms the hexagonal structure of the APCVD-grown $MoSe_2$. In light of this observation, we repeated the defect formation energy calculations while preserving the simulation cell shape, in order to conserve the experimentally confirmed hexagonal structure. The "fixed cell" formation energies of our DFT calculations, presented in Figure 3a, in combination with the experimental observations, indicate that Mo_{int} is the most energetically favorable interstitial atom and the most likely to exist in our APCVD-grown $MoSe_2$ samples. Note that the "fixed cell" calculations are for qualitative comparison purposes, and used to estimate the energetics of Se_{int} in hexagonal $MoSe_2$. Figure 3b shows the optimized atomic structure of a $3 \times 3 \times 1$ $MoSe_2$ supercell with one Mo_{int}, where the Mo_{int} is found to preferentially reside at the high-symmetry point equidistant to six Se nearest neighbors (2.5 Å bond length). The electronic structure of a $4 \times 4 \times 1$ $MoSe_2$ supercell with one Mo_{int} is presented in Figure 3c. The interstitial Mo introduces filled mid-gap states located between –0.3 and 0 eV relative to the Fermi level (for comparison, the band structure of pure $MoSe_2$ is provided in Figure S5 in the Supporting Information). The contribution from the Mo_{int} d-orbitals is indicated in Figure 3d, confirming the interstitial atom as the source of the mid-gap bands (s- and p-orbitals have much less contribution). In addition, we note that, unlike Mo_{int}, our DFT electronic structure calculations show that Se_{int} does not introduce mid-gap states (see Figure S6 in the Supporting Information), and hence would not be expected to improve the photoresponsivity.

Finally, our DFT results suggest that Se_{vac} is another defect that could potentially exist in $MoSe_2$ (although the Raman spectrum of our APCVD-grown multilayer $MoSe_2$ suggests the absence of Se_{vac} based on a previous report[16]). Figure 3e presents the electronic structure of a $4 \times 4 \times 1$ $MoSe_2$ supercell with one Se_{vac}. We find both Mo_{int} and Se_{vac} introduce gap states, however an important distinction is that with Mo_{int} and Se_{vac}, the gap states are filled and empty, respectively. In the case of Se_{vac}, unoccupied gap states (or equivalently occupied with holes) prevent holes from being trapped by those states, which impedes the photovoltaic effect – a key mechanism observed with the $MoSe_2$ phototransistor. With Mo_{int}, the gap states are filled (empty of holes), and thus can trap holes and contribute significantly to the photovoltaic effect. Therefore, we can conclude that Mo_{int} is the key element that can most significantly contribute to the photovoltaic effect and the large photoresponsivity in multilayer $MoSe_2$ phototransistors.

We also confirmed the larger number of gap states in the synthetic $MoSe_2$ compared to natural MoS_2 through direct measurements of photoinduced transfer characteristics. **Figure 4**a,b

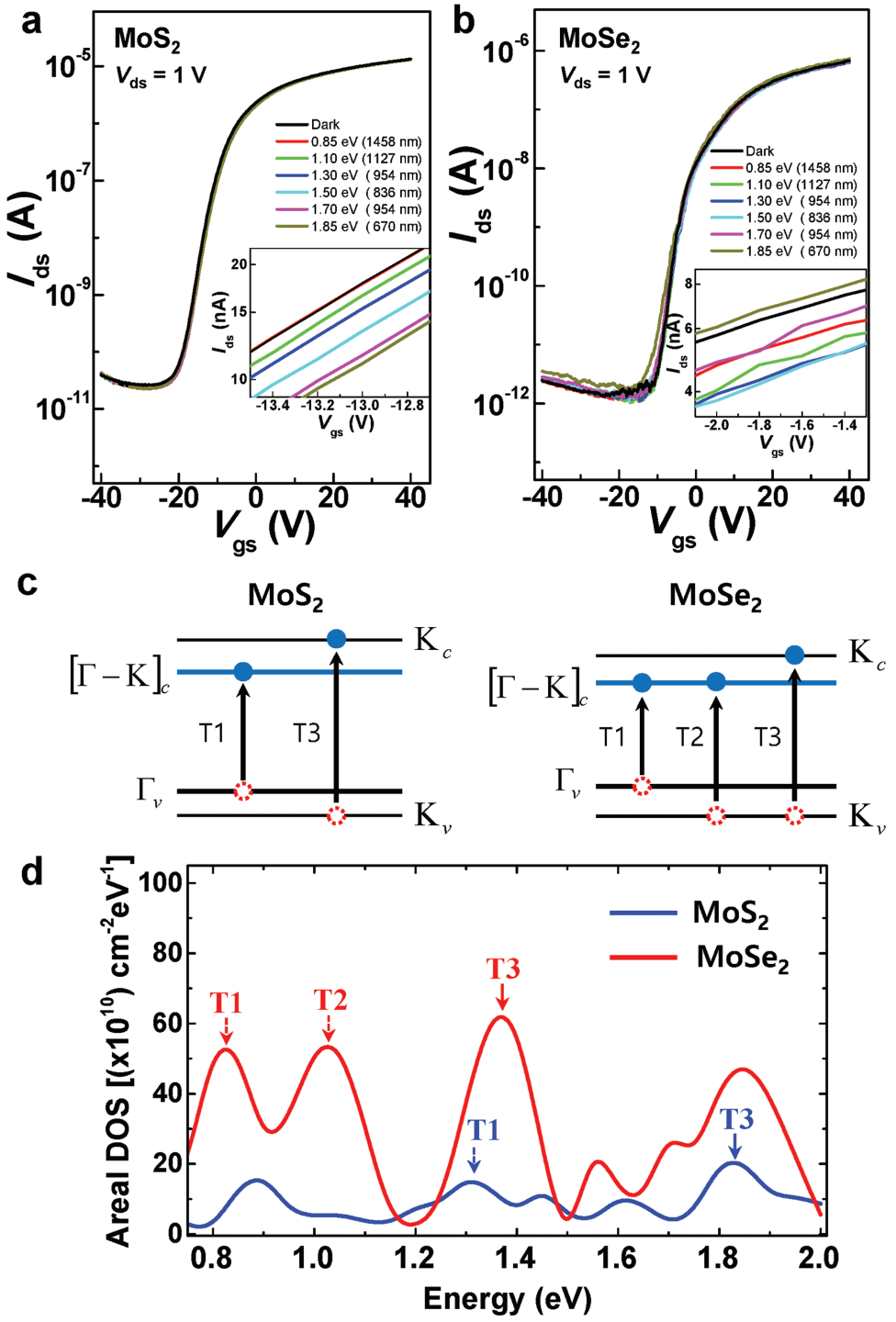

Figure 4. Photoinduced spectral response of MoS_2 and $MoSe_2$ phototransistors. a,b) Photoinduced $I_{ds} - V_{gs}$ curves of the (a) MoS_2 and (b) $MoSe_2$ TFTs under monochromatic light radiation with various wavelengths. c) Interband transitions plotted in the simplified energy diagram of MoS_2 (left) and $MoSe_2$ (right). Γ_v and $|\Gamma - K|_c$ denote valence band maxima and conduction band minima without spin-orbit coupling (SOC) effects, respectively, and K_v and K_c denote valence band and conduction band edge at K point, respectively. d) Photon energy-dependent areal DOS profiles of MoS_2 and $MoSe_2$ TFTs. The profiles reflect the different band-to-band transitions for MoS_2 and $MoSe_2$ TFTs, and the areal DOS is significantly larger in $MoSe_2$ than in MoS_2.

shows the I_{ds}–V_{gs} curves of the MoS_2 and $MoSe_2$ TFTs, respectively, under monochromatic light radiation with various wavelengths in the linear regime. Seemingly, there are little changes in threshold voltages and off-state current for both the MoS_2 and $MoSe_2$ TFTs. However, a close look on the insets of Figure 4a indicates that the threshold voltage of MoS_2 TFT shifts toward

positive values with increasing incident photon energy (i.e., decreasing wavelength). The positive shift of the threshold voltage under illumination of light could be counterintuitive as one would usually expect negative shifts owing to the generation of excess carriers. However, the positive shift in threshold voltage may have resulted from the bias-stress effect induced by the continued photoinduced transfer curve measurements on the device, which in general results in current drop at a fixed gate voltage.[17] Notably, the presence of defects at the interface between the 300 nm thick silicon dioxide (SiO_2) insulator and the TMD channel in TFTs will be inevitable. In such a case, when the gate bias is continuously applied, some of the charges can be trapped by the defects at the interface, resulting in the positive shift of V_{th} and the bias-stress effect. In light of this, it may be suggested that the MoS_2 TFT is relatively insensitive to the illumination of light, which cannot fully compensate the bias-stress effects. Unlike the MoS_2 TFTs, the threshold voltages of $MoSe_2$ TFTs shift toward negative values, as shown in the insets of Figure 4b, in the photon energy ranges of 1.10–1.35 and 1.50–1.70 eV (see also Figure S7 in the Supporting Information), indicating the remarkable interband charge transitions, as illustrated by the schematic energy diagrams in Figure 4c. Figure 4d shows the areal DOS profiles of both MoS_2 and $MoSe_2$ TFTs extracted from the ΔV_{th} dependent curves by differentiating the excited charge values with the incident photon energy (Figure S7, Supporting Information). The spectral DOS profiles exhibit charge transition peaks with the DOS in the energy range depicted by T1 (≈1.30 eV) and T3 (≈1.85 eV) for MoS_2 and T1 (≈0.85 eV), T2 (≈1.10 eV), and T3 (≈1.34 eV) for $MoSe_2$, which match well with the previously reported values with only minor deviations.[4d,18] A summary of the interband transitions near the bandgap for both bulk MoS_2 and bulk $MoSe_2$ is presented in Table 1. Note that the assigned energy states in our APCVD-grown multilayer $MoSe_2$ films have significantly larger areal DOS than the ones in the natural MoS_2 flakes. It is thus inferred that the $MoSe_2$ has a much larger number of energy states that can act as charge traps, as depicted in the inset of Figure 2e. Some peaks in the spectrum of Figure 4d could not be assigned to any particular state; for example, those arising at ≈0.90 and ≈1.65 eV for MoS_2, and at ≈1.55 and ≈1.85 eV for $MoSe_2$. However, given the energy state level, it may be suggested that the peak at ≈0.90 eV in MoS_2 is related to the subgap states in the energy bands and the peak at ≈1.65 eV corresponds to the interband transition in bilayer MoS_2, while the peaks at ≈1.55 and ≈1.85 eV in $MoSe_2$ are related to the charge transitions in the higher energy states.[4d,18a]

In the present work, the fundamental origin of high photoresponsivity in synthetic $MoSe_2$ phototransistors was sought.

Table 1. Band-to-band transitions near the gap in bulk $MoSe_2$ and bulk MoS_2.

Label	Transition	Transition energy [eV]	
		$MoSe_2$	MoS_2
T1	$\Gamma_v \rightarrow \lvert\Gamma - K\rvert_c$	0.85	1.30
T2	$K_v \rightarrow \lvert\Gamma - K\rvert_c$	1.10	–
T3	$K_v \rightarrow K_c$	1.34	1.85

Aberration-corrected HRTEM images confirmed the existence of interstitial atoms in synthetic multilayer $MoSe_2$, and it was revealed that such interstitials are Mo_{int} rather than Se_{int} based on DFT calculations. DFT results further exhibited the formation of gap states due to the Mo_{int}, and the measurements of photoinduced transfer characteristics also confirmed significantly large subgap states in the synthetic $MoSe_2$, unlike typical MoS_2 flakes. The photoresponsive characteristics were analyzed by models, which indicated that Mo_{int}-induced gap states are the fundamental origin of significant PV effects, leading to large photoresponsivity in synthetic multilayer $MoSe_2$ phototransistors. The results presented in this work will provide a significant practical advancement in the field of multifunctional 2D electronics for wearable sensor applications.[19]

Experimental Section

Synthesis and Device Fabrication: The single-crystalline $MoSe_2$ platelets were fabricated through the modified APCVD method based on direct vapor transport of seed materials.[20] First, the polycrystalline $MoSe_2$ compounds were prepared through solid state reaction,[21] and utilized as precursor (p-$MoSe_2$).[20a] To optimize the wettability of the single-crystalline $MoSe_2$, a thin layer of molybdenum (Mo) with a thickness of 10 nm was deposited on a silicon (Si) substrate. Then, p-$MoSe_2$ compounds and Mo-coated Si substrates were placed at the hot and cold zones of the evacuated quartz ampoule, and the reaction temperatures were slowly increased up to 1050 and 1000 °C, respectively.

In order to fabricate phototransistors, multilayer $MoSe_2$ flakes were mechanically exfoliated from single-crystalline platelets, and transferred onto n-type doped Si substrates covered with a 300 nm thick SiO_2 as the gate insulator. Titanium/gold layers with respective thicknesses of 15/300 nm were deposited by electron beam evaporation. Then, S/D electrodes were patterned through conventional photolithography and etching procedures. To improve the contact resistance, the phototransistor was thermally annealed in a furnace at 200 °C for 2 h under gas flow conditions (100 sccm Ar and 10 sccm H_2). For quantitative comparisons, multilayer MoS_2 phototransistors were also fabricated based on the above procedure using mechanically exfoliated flakes from bulk crystals (SPI supplies, USA). Details of synthesis and device fabrication were reported earlier.[4b,5,20a]

Characterization: Morphologies of the APCVD-grown $MoSe_2$ layers were characterized by STEM (JEM-ARM200F, Jeol) and HRTEM (FEI Titan Cubed G^2 60-300).

The electrical properties of APCVD-grown $MoSe_2$ phototransistors were investigated using a Keithley 4200-SCS semiconductor characterization system equipped with a probe station at room temperature under ambient conditions. Radiations with various wavelengths were generated with a Multichannel Fiber-Coupled Laser Source (MCLS1, Thorlabs), and guided in a direction perpendicular to the active channel of the phototransistors via Single Mode Fiber Optic Patch Cables (S405-HP for 405 nm, SM600 for 638 nm, and SM800 for 852 nm, Thorlabs). Power densities of the incident light were measured using a Standard Photodiode Power Sensor (S120VC, Thorlabs), connected to an Analog Handheld Laser Power Meter Console (PM100A, Thorlabs).

In order to measure the photoinduced transfer curves of the TFTs, the electrical measurements were performed under an intense monochromatic light (photon flux of at least 5×10^{14} cm^{-2} s^{-1} as estimated from the optical power density, ≈0.1 mW cm^{-2}). The optical spectroscopic system is equipped with a light source of 500 W Hg(Xe) arc lamp, a grating monochromator covering a spectral range of 300–1000 nm and an optical fiber (core diameter of 200 µm) as an optical probe that guides photons to the channel area of the testing device, which is connected to an electrical measurement unit (4155C Semiconductor Parameter Analyzer, Agilent Technologies).

Model: To calculate the conductivity increase due to illumination, a modified Hornbeck–Haynes model is used as $\Delta\sigma = q(\mu_n + \mu_p)\Delta p + q\mu_n p_t$, where μ_n and μ_p are the electron and hole mobilities, respectively, Δp is the excess hole density in the valence band, and p_t is the trapped hole density.[10] The mobilities of 97.4 and 16.6 $cm^2\ V^{-1}\ s^{-1}$ are extracted from the experiments and used for $MoSe_2$ and MoS_2 TFTs, respectively, and Δp is obtained by $\Delta p = g\tau_r$, where g ($= \eta P_{abs}/h\nu$) is the generation rate of photons and τ_r is the carrier recombination lifetime (fitted). η and $h\nu$ are the internal quantum efficiency and the single photon energy, respectively. The internal quantum efficiency is chosen as η = 0.5, 0.5, 0.07 for λ_{ex} = 405, 638, 852 nm, respectively. P_{abs} is the absorbed power density, given by $P_{inc}\left(1 - \frac{e^{-\alpha^{\perp}d} + e^{-\alpha^{\parallel}d}}{2}\right)$, where $\alpha^{\perp}$ and $\alpha^{\parallel}$ are the absorption coefficient in the vertical ($\alpha^{\perp} = 28.3 \times 10^4\ cm^{-1}$ at λ_{ex} = 405 nm, $1.22 \times 10^4\ cm^{-1}$ at 638 nm, $4.88 \times 10^3\ cm^{-1}$ at 852 nm for $MoSe_2$; $26.6 \times 10^4\ cm^{-1}$ at 405 nm for MoS_2)[22] and lateral direction ($\alpha^{\parallel} = 103.4 \times 10^4\ cm^{-1}$ at λ_{ex} = 405 nm, $10.3 \times 10^4\ cm^{-1}$ at 638 nm, $1.37 \times 10^4\ cm^{-1}$ at 852 nm for $MoSe_2$; $87.1 \times 10^4\ cm^{-1}$ at 405 nm for MoS_2),[22] respectively, and d is the thickness of channel material (d = 60 nm for $MoSe_2$; 40 nm for MoS_2). The trapped hole density is calculated by $p_t = (gP_t\tau_r)/(g\tau_r + P_t(\tau_t/\tau_g))$, where P_t is the trap density, and τ_t and τ_g are the trapping and escaping times of holes into and from the trap states, respectively.[10] Photoconductive current ($I_{ph,PC}$) is obtained in the off state (V_{gs} = −40 V) from the measurement data (Figure 2a,b and Figure S3 (Supporting Information)) and fitted with $I_{ph,PC} = \left(\frac{W}{L}\right)V_{ds}\,\Delta\sigma$ in Figure 2d, resulting in the following fitting parameters: $P_t = 5 \times 10^{10}\ cm^{-2}$, τ_r = 150 ps, and τ_t/τ_g = 1/1000 for $MoSe_2$; $P_t = 3 \times 10^{10}\ cm^{-2}$, τ_r = 8 ns, and τ_t/τ_g = 1/100 for MoS_2. To evaluate the PV effect below, τ_g of 10 and 1 ns are assumed for $MoSe_2$ and MoS_2, respectively. W/L is 8.3 µm/13.1 µm for $MoSe_2$; 63 µm/15.1 µm for MoS_2.

On the other hand, the PV effect is modeled with the threshold voltage shift (ΔV_{th}) due to potential barrier lowering ($\Delta\phi_b$), considering that ΔV_{th} is proportional to $\Delta\phi_b$.[11] When positive charges are locally accumulated inside the device, potential barrier for electrons can be lowered, in which the potential energy varies linearly while the amount of charges changes exponentially.[23] Therefore, the barrier lowering can be modeled as $\Delta\phi_b = n\frac{k_B T}{q}\ln\left(\frac{qp}{\tau_{eff} J_{pd}}\right)$, where k_B, T, q, J_{pd}, τ_{eff}, and n are the Boltzmann constant, the temperature, the unit charge, the dark hole current, the effective lifetime, and a constant accounting for the saturation effect, respectively.[23] The number of holes (p) can be expressed as $\frac{p}{\tau_{eff}} = \frac{J_{pd}}{q} + \frac{P_{abs}\eta}{h\nu} + \frac{p_t}{\tau_g}$, where $\frac{J_{pd}}{q}$, $\frac{P_{abs}\eta}{h\nu}$, and $\frac{p_t}{\tau_g}$ correspond to the background charge (in dark), the excess carriers in the valence band due to the illumination, and the trapped charges in subgap states, respectively. Considering hole accumulation, barrier lowering, and threshold voltage shift all together, the photovoltaic current can be determined by $I_{ph,PV} = g_m\Delta V_{th} = \chi_{BL} g_m \frac{k_B T}{q}\ln\left(1 + \frac{P_{abs}\eta q}{h\nu J_{pd}} + \frac{p_t q}{\tau_g J_{pd}}\right)$, where χ_{BL} is the barrier-lowering efficiency, the only fitting parameter for the PV effect, which is directly related to the trap density and also to the wavelength of incident light. χ_{BL} = 25, 19.5, 9 are used for λ_{ex} = 405, 638, 852 nm, respectively, and $g_m = 4.55 \times 10^{-7}$ S for $MoSe_2$; χ_{BL} = 2.5 at λ_{ex} = 405 nm and $g_m = 6.64 \times 10^{-7}$ S for MoS_2. The fitted values of χ_{BL} suggest that the trap density in $MoSe_2$ is significantly larger than that of MoS_2, which is consistent with P_t values determined for the PC effect above and also with DFT simulation results and the measurements of photoinduced transfer characteristics. For n-type transistors considered in this study, it is assumed that J_{pd} is less than the dark electron current density (J_{nd}) by three orders of magnitude.

DFT Simulations: The DFT calculations were performed using the Vienna *ab initio* simulation package (VASP).[24] A plane-wave expansion cutoff energy of 450 eV for the wave function, the projector augmented wave method for the treatment of the core potential, and the local density approximation (LDA) for exchange-correlation potential were used.[25] LDA is known to underestimate bandgap and lattice constant values, however the qualitative results and conclusions from the DFT calculations should hold true. Spin–orbit coupling (SOC) was not included in the presented results, however a test with spin–orbit interaction activated showed no qualitative differences. For pure bulk $MoSe_2$, a Monkhorst–Pack G-centered k-grid of 8 × 8 × 2 was used. The optimized lattice constants of the hexagonal structure are a = 3.25 Å and c = 12.73 Å, obtained using a total energy convergence of 10^{-6} eV and with forces acting on each atom less than 0.01 eV $Å^{-1}$. van der Waals interaction was omitted, but is not expected to alter the conclusions since the optimized lattice constants of pristine $MoSe_2$ are within 2% of the experimental values[26] and that the interstitial defects form strong bonds with the neighboring $MoSe_2$ layers.

The defect calculations are performed by (i) introducing each defect into a 4 × 4 × 1 supercell of $MoSe_2$ (96 atoms without the defects), (ii) relaxing the atomic structure using the same criteria described above, and (iii) performing a self-consistent calculation to extract the total energy. The defect formation energies are calculated using $E_f = E_{defect} - (E_{pristine} \pm \mu_i)$, where E_f is the formation energy, E_{defect} is the total energy of the supercell with the defect, $E_{pristine}$ is the total energy of the pristine supercell without the defect, μ_i is the chemical potential of element i (+ is used if element i is added to the pristine supercell to form the defect, and − is used if element i is removed from the pristine supercell to form the defect).[13] The chemical potentials, μ_i, are obtained from $E_{MoSe_2} = \mu_{Mo} + 2\mu_{Se}$, where E_{MoSe_2} is the total energy of the pristine material per unit formula $MoSe_2$. μ_{Mo} and μ_{Se} are determined by $\mu_{Mo} = E_{Mo}$ and $\mu_{Se} = (E_{MoSe_2} - \mu_{Mo})/2$, where E_{Mo} is the total energy per atom of a body-centered cubic (BCC) crystal of Mo (the stable/common bulk form of Mo), considering Mo-rich condition. For the 4 × 4 × 1 supercell calculations with a defect, a Monkhorst–Pack G-centered k-grid of 2 × 2 × 2 was used. The optimized lattice constants of the supercell with 1% Mo_{int} are a = 3.25 Å and c = 12.99 Å, obtained using the same convergence criteria as with the primitive cell. At the start of the atomic relaxation, the interstitial Mo atom was randomly displaced slightly away from the high-symmetry location where it finally settled at a high-symmetry point that is equidistant to the six Se nearest neighbors with a bond distance of 2.50 Å.

Supporting Information

Supporting Information is available from the Wiley Online Library or from the author.

Acknowledgements

S.K., J.M., J.L., and S.M.K. contributed equally to this work. This research was supported in part by the National Research Foundation of Korea (Grants NRF-2015R1A5A1037548, NRF-2014M3A9D7070732, NRF-2013M3C1A3059590, NRF- 2015R1C1A1A02037534), the NSERC Discovery Grants of Canada (RGPIN-05920-2014 and RGPIN-2016-04881), and the Commercializations Promotion Agency for R&D Outcomes (COMPA) funded by the Ministry of Science, ICT and Future Planning (MISP). This study was also supported in part by the grants from the Korea Institute of Science and Technology (KIST) institutional program. G.H. acknowledges the financial support by the NSERC Canada Graduate Scholarships Program and the WIN Nanofellowship.

Conflict of Interest

The authors declare no conflict of interest.

Keywords

2D materials, interstitial effects, $MoSe_2$, phototransistors, photovoltaics

Received: September 25, 2017
Revised: November 26, 2017
Published online:

[1] a) D. Jariwala, V. K. Sangwan, L. J. Lauhon, T. J. Marks, M. C. Hersam, *ACS Nano* **2014**, *8*, 1102; b) M. Buscema, J. O. Island, D. J. Groenendijk, S. I. Blanter, G. A. Steele, H. S. J. van der Zant, A. Castellanos-Gomez, *Chem. Soc. Rev.* **2015**, *44*, 3691; c) H. Schmidt, F. Giustiniano, G. Eda, *Chem. Soc. Rev.* **2015**, *44*, 7715; d) S. L. Li, K. Tsukagoshi, E. Orgiu, P. Samorì, *Chem. Soc. Rev.* **2016**, *45*, 118.

[2] a) Q. H. Wang, K. Kalantar-Zadeh, A. Kis, J. N. Coleman, M. S. Strano, *Nat. Nanotechnol.* **2012**, *7*, 699; b) M. Chhowalla, H. S. Shin, G. Eda, L. J. Li, K. P. Loh, H. Zhang, *Nat. Chem.* **2013**, *5*, 263; c) Y. Zhang, T. R. Chang, B. Zhou, Y. T. Cui, H. Yan, Z. Liu, F. Schmitt, J. Lee, R. Moore, Y. Chen, H. Lin, H. T. Jeng, S. K. Mo, Z. Hussain, A. Bansil, Z. X. Shen, *Nat. Nanotechnol.* **2014**, *9*, 111.

[3] a) Y. Yu, Z. Ji, S. Zu, B. Du, Y. Kang, Z. Li, Z. Zhou, K. Shi, Z. Fang, *Adv. Funct. Mater.* **2016**, *26*, 6394; b) B. Li, S. Zu, J. Zhou, Q. Jiang, B. Du, H. Shan, Y. Luo, Z. Liu, X. Zhu, Z. Fang, *ACS Nano* **2017**, *11*, 9720; c) Z. Li, Y. Li, T. Han, X. Wang, Y. Yu, B. Tay, Z. Liu, Z. Fang, *ACS Nano* **2017**, *11*, 1165.

[4] a) J. Kwon, Y. K. Hong, G. Han, I. Omkaram, W. Choi, S. Kim, Y. Yoon, *Adv. Mater.* **2015**, *27*, 2224; b) W. Choi, M. Y. Cho, A. Konar, J. H. Lee, G. B. Cha, S. C. Hong, S. Kim, J. Kim, D. Jena, J. Joo, *Adv. Mater.* **2012**, *24*, 5832; c) K. F. Mak, C. Lee, J. Hone, J. Shan, T. F. Heinz, *Phys. Rev. Lett.* **2010**, *105*, 136805; d) S. Tongay, J. Zhou, C. Ataca, K. Lo, T. S. Matthews, J. Li, J. C. Grossman, J. Wu, *Nano Lett.* **2012**, *12*, 5576.

[5] S. Kim, A. Konar, W. S. Hwang, J. H. Lee, J. Lee, J. Yang, C. Jung, H. Kim, J. B. Yoo, J. Y. Choi, Y. W. Jin, S. Y. Lee, D. Jena, W. Choi, K. Kim, *Nat. Commun.* **2012**, *3*, 1011.

[6] a) A. Abderrahmane, P. J. Ko, T. V. Thu, S. Ishizawa, T. Takamura, A. Sandhu, *Nanotechnology* **2014**, *25*, 365202; b) W. Zhang, Q. Wang, Y. Chen, Z. Wang, A. T. S. Wee, *2D Mater.* **2016**, *3*, 022001; c) L. Zheng, L. Zhongzhu, S. Guozhen, *J. Semicond.* **2016**, *37*, 091001; d) C. Jung, S. M. Kim, H. Moon, G. Han, J. Kwon, Y. K. Hong, I. Omkaram, Y. Yoon, S. Kim, J. Park, *Sci. Rep.* **2015**, *5*, 15313.

[7] a) J. Lu, J. H. Lu, H. Liu, B. Liu, K. X. Chan, J. Lin, W. Chen, K. P. Loh, C. H. Sow, *ACS Nano* **2014**, *8*, 6334; b) D. S. Tsai, K. K. Liu, D. H. Lien, M. L. Tsai, C. F. Kang, C. A. Lin, L. J. Li, J. H. He, *ACS Nano* **2013**, *7*, 3905; c) G. Cunningham, U. Khan, C. Backes, D. Hanlon, D. McCloskey, J. F. Donegan, J. N. Coleman, *J. Mater. Chem. C* **2013**, *1*, 6899.

[8] H. Oswald, R. Asper, R. Lieth, *Preparation and Crystal Growth of Materials with Layered Structures*, D. Reidel Publishing Company, Dordrecht **1977**.

[9] a) HQgraphene (Netherlands), http://www.hqgraphene.com (accessed: Jan. 2017); b) Sigma-Aldrich (United States), http://www.sigmaladrich.com (accessed: Jan. 2017).

[10] M. M. Furchi, D. K. Polyushkin, A. Pospischil, T. Mueller, *Nano Lett.* **2014**, *14*, 6165.

[11] Y. Takanashi, K. Takahata, Y. Muramoto, *IEEE Electron Device Lett.* **1998**, *19*, 472.

[12] A. R. Jha, *Infrared Technology*, Wiley, New York **2000**.

[13] S. Haldar, H. Vovusha, M. K. Yadav, O. Eriksson, B. Sanyal, *Phys. Rev. B* **2015**, *92*, 235408.

[14] Y. Kang, Y. Gong, Z. Hu, Z. Li, Z. Qiu, X. Zhu, P. M. Ajayan, Z. Fang, *Nanoscale* **2015**, *7*, 4482.

[15] Y. Kang, S. Najmaei, Z. Liu, Y. Bao, Y. Wang, X. Zhu, N. J. Halas, P. Nordlander, P. M. Ajayan, J. Lou, Z. Fang, *Adv. Mater.* **2014**, *26*, 6467.

[16] M. Mahjouri-Samani, L. Liang, A. Oyedele, Y.-S. Kim, M. Tian, N. Cross, K. Wang, M.-W. Lin, A. Boulesbaa, C. M. Rouleau, A. A. Puretzky, K. Xiao, M. Yoon, G. Eres, G. Duscher, B. G. Sumpter, D. B. Geohegan, *Nano Lett.* **2016**, *16*, 5213.

[17] K. Cho, W. Park, J. Park, H. Jeong, J. Jang, T. Y. Kim, W. K. Hong, S. Hong, T. Lee, *ACS Nano* **2013**, *7*, 7751.

[18] a) T. Cheiwchanchamnangij, W. R. L. Lambrecht, *Phys. Rev. B* **2012**, *85*, 205302; b) A. R. Beal, H. P. Hughes, *J. Phys. C: Solid State Phys.* **1979**, *12*, 881.

[19] a) J. Pu, Y. Yomogida, K. K. Liu, L. J. Li, Y. Iwasa, T. Takenobu, *Nano Lett.* **2012**, *12*, 4013; b) G. A. Salvatore, N. Münzenrieder, C. Barraud, L. Petti, C. Zysset, L. Büthe, K. Ensslin, G. Tröster, *ACS Nano* **2013**, *7*, 8809; c) W. G. Song, H.-J. Kwon, J. Park, J. Yeo, M. Kim, S. Park, S. Yun, K.-U. Kyung, C. P. Grigoropoulos, S. Kim, Y. K. Hong, *Adv. Funct. Mater.* **2016**, *26*, 2426; d) H. Y. Chang, M. N. Yogeesh, R. Ghosh, A. Rai, A. Sanne, S. Yang, N. Lu, S. K. Banerjee, D. Akinwande, *Adv. Mater.* **2016**, *28*, 1818.

[20] a) J.-S. Rhyee, J. Kwon, P. Dak, J. H. Kim, S. M. Kim, J. Park, Y. K. Hong, W. G. Song, I. Omkaram, M. A. Alam, S. Kim, *Adv. Mater.* **2016**, *28*, 2316; b) C. K. Sumesh, K. D. Patel, V. M. Pathak, R. Srivastav, *Cryst. Res. Technol.* **2010**, *45*, 957.

[21] E. Revolinsky, D. Beerntsen, *J. Appl. Phys.* **1964**, *35*, 2086.

[22] U. Ahuja, R. Joshi, D. Kothari, H. Tiwari, K. Venugopalan, *Z. Naturforsch., A: Phys. Sci.* **2016**, *71*, 213.

[23] C. Y. Chen, *Appl. Phys. Lett.* **1981**, *39*, 979.

[24] a) G. Kresse, J. Furthmüller, *Phys. Rev. B* **1996**, *54*, 11169; b) G. Kresse, J. Furthmüller, *Comput. Mater. Sci.* **1996**, *6*, 15.

[25] a) J. P. Perdew, A. Zunger, *Phys. Rev. B* **1981**, *23*, 5048; b) D. M. Ceperley, B. J. Alder, *Phys. Rev. Lett.* **1980**, *45*, 566.

[26] P. B. James, M. T. Lavik, *Acta Crystallogr.* **1963**, *16*, 1183.